


Nonperturbatively renormalized nucleon gluon momentum fraction in the continuum limit of $N_f = 2 + 1 + 1$ lattice QCD

Zhouyou Fan,¹ Huey-Wen Lin^{1,2} and Matthew Zeilbeck¹

¹*Department of Physics and Astronomy, Michigan State University, East Lansing, Michigan 48824, USA*

²*Department of Computational Mathematics, Science and Engineering, Michigan State University, East Lansing, Michigan 48824, USA*

 (Received 23 August 2022; accepted 12 January 2023; published 14 February 2023)

We present the nonperturbatively renormalized nucleon gluon momentum fraction using ensembles with $2 + 1 + 1$ flavors of highly improved staggered quarks (HISQ), generated by the MILC Collaboration. The calculation is done using clover fermions for the valence action with three pion masses, 220, 310, and 690 MeV, and three lattice spacings, 0.09, 0.12, and 0.15 fm. The renormalization is done using RI/MOM nonperturbative renormalization and using cluster-decomposition error reduction (CDER) to enhance the signal-to-noise ratio of the renormalization constant. We find the CDER technique is particularly important to improve the signal at the finer lattice ensembles where the lattice volume is larger. We extrapolate the gluon momentum fraction to the continuum-physical limit and obtain $\langle x \rangle_g = 0.502(53)_{\text{stat+NPR}}(50)_{\text{mixing}}$ in the $\overline{\text{MS}}$ scheme at 2 GeV, where first error includes the statistical error and uncertainties in nonperturbative renormalization, while the latter systematic error accounts for ignoring quark mixing. Our gluon momentum fraction is consistent with other recent lattice-QCD results at physical pion mass.

DOI: [10.1103/PhysRevD.107.034505](https://doi.org/10.1103/PhysRevD.107.034505)

I. INTRODUCTION

The gluon momentum fraction $\langle x \rangle_g$ of the nucleon is important to particle and nuclear physics. It can be measured as the momentum fraction carried by gluons in the infinite momentum frame and must satisfy the momentum sum rule $\langle x \rangle_g + \langle x \rangle_q = 1$ with the sum of the quark momentum fraction. These momentum fractions are key inputs to understanding the proton mass and spin decomposition, which are major outstanding questions in hadronic physics. The gluon momentum fraction is connected to the unpolarized nucleon gluon parton distribution function (PDF) $g(x)$ via

$$\langle x \rangle_g = \int_0^1 dx x g(x). \quad (1)$$

The gluon PDF is an important input to many theory predictions used in the hadron colliders [1–8]. For example, $g(x)$ needs to be known precisely to calculate the cross section for processes in pp collisions, including the cross section for Higgs-boson production and jet production at the Large Hadron Collider (LHC) [9,10]. Ongoing and

future experiments, such as new experiments at the Jefferson Lab 12-GeV facility and the U.S.-based Electron-Ion Collider (EIC) [11], planned to be built at Brookhaven National Lab, will further our knowledge of the gluon PDF [12–14].

Lattice quantum chromodynamics (lattice QCD or LQCD) is a theoretical method that can provide full systematic control in calculating QCD quantities in the nonperturbative regime and can provide useful information for improving our knowledge of the gluon structure of the nucleon, independent from experiments. There have been many lattice calculations of the nucleon quark momentum fraction $\langle x \rangle_q$ (see reviews in Refs. [15,16]), but still relatively few attempts for the gluon counterpart [17–20]. This is mainly due to the fact that any gluon observable on the lattice is extremely noisy. Furthermore, the renormalization for even the gluon-only momentum fraction has been difficult to calculate nonperturbatively (at large volumes). Early lattice-QCD studies calculated $\langle x \rangle_g$ of the nucleon on quenched lattices using heavy pion masses and gave $\langle x \rangle_g \in [0.3, 0.6]$ [17–20]. There have been a number of dynamical calculations of the gluon momentum fraction of the nucleon using 2-flavor (degenerate up and down sea quarks), $2 + 1$ -flavor (including strange quark), and $2 + 1 + 1$ -flavor (including charm quark) lattice calculations by ETMC, χ QCD, and MIT lattice groups [21–25]; see the summary in Table I. Additional smearing and large numbers of statistical measurements are typically

Published by the American Physical Society under the terms of the Creative Commons Attribution 4.0 International license. Further distribution of this work must maintain attribution to the author(s) and the published article's title, journal citation, and DOI. Funded by SCOAP³.

TABLE I. Summary of lattice dynamical calculations of the nucleon gluon moment sorted by year. The columns from left to right show for each calculation: the number of flavors of quarks in the QCD vacuum (N_f), the lattice spacing (a) in fm, the valence pion mass (M_π^{val}) in MeV, the valence fermion action (“Fermion”), where “TM” stands for twisted-mass fermion action, the number of measurements of the nucleon correlators (N_{meas}), the renormalization method (“Renorm.”) indicating 1-loop perturbative calculations or RI-MOM nonperturbative renormalization, the smearing technique used to improve the gluon signals (“G smearing”), and the obtained gluon momentum fraction ($\langle x \rangle_g$) renormalized at 2-GeV scale in $\overline{\text{MS}}$ scheme. The lattice errors coming from different sources are marked as “stat.” for statistical, “cont.” for continuum-extrapolation (or lack thereof), “ES” for excited state contamination (but later calculations remove them, folding this error into the statistical), “PT” for perturbative renormalization, “NPR” for nonperturbative renormalization, and “mixing” for the mixing with the quark sector.

Group	N_f	a (fm)	M_π^{val} (MeV)	Fermion	N_{meas}	Renorm.	G smearing	$\langle x \rangle_g$
ETMC16 [21]	2 + 1 + 1	0.08	370	TM	34,470	1-loop	2-stout	0.284(27) _{stat.} (17) _{ES} (24) _{PT}
ETMC16 [21]	2	0.09	131	TM	209,400	1-loop	2-stout	0.267(22) _{stat.} (19) _{ES} (24) _{PT}
ETMC17 [22]	2	0.09	131	TM	209,400	1-loop	2-stout	0.267(12) _{stat.} (10) _{ES}
MIT18 [23]	2 + 1	0.12	450	Clover	572,663	RI-MOM	Wilson flow	0.54(8) _{stat.}
χ QCD18a [24]	2 + 1	0.114	[135, 372] ^a	Overlap	81 cfgs	RI-MOM	1-HYP	0.47(4) _{stat.} (11) _{NPR+mixing}
χ QCD18b [26]	2 + 1	[0.08, 0.14]	[140,400]	Overlap	[81, 309] cfgs	RI-MOM	1-HYP	0.482(69) _{stat.} (48) _{cont.}
ETMC20 [25]	2 + 1 + 1	0.08	139.3	TM	48,000	1-loop	10-stout	0.427(92) _{stat.}
χ QCD21 [27]	2 + 1	0.14	[171, 391] ^b	Overlap	8,200	RI-MOM	1-HYP	0.509(20) _{stat.} (23) _{cont.}
MSULat22 (this work)	2 + 1 + 1	[0.09,0.15]	[220,700] ^c	Clover	10 ⁵ –10 ⁶	RI-MOM	5-HYP	0.502(53) _{stat.+NPR} (50) _{mixing}

^aPartially quenched calculation on domain-wall fermion $M_\pi^{\text{sea}} = 140$ -MeV lattice.

^bPartially quenched calculation on domain-wall fermion $M_\pi^{\text{sea}} = 171$ -MeV lattice.

^cClover-on-HISQ mixed action with valence pion masses tuned to lightest sea-quark ones.

needed to produce a usable gluon signal. Since 2018, χ QCD and MIT lattice groups have used nonperturbative renormalization on the gluon operators. There has been an attempt by χ QCD to study the lattice-spacing dependence using 2 + 1-flavor ensembles using partially quenched mixed actions (where the valence pion masses are allowed to be different from the sea pion masses). Although progress has been made in recent years, there is still disagreement between the lattice determination of the gluon momentum fraction and those obtained from taking the integral of the global-fit gluon PDF in Eq. (1). Reference [15] quoted numbers from multiple gluon PDF determinations (NNPDF3.1, CT14, MMHT14, ABMP16, CJ15, and HERAPDF2.0), yielding a weighted-average gluon momentum fraction of 0.411(8). Since then, JAM19 and CT18 have published updated values, 0.403(2) and 0.413(8), respectively. More lattice studies are needed to understand the potential discrepancy between lattice calculations and global-fit results.

The gluon momentum fraction remains an important calculation target despite recent developments in pseudo-PDF [28] and quasi-PDF [29,30] approaches, which have opened up opportunities to calculate the full x dependence of the gluon PDF. The first attempt to determine the nucleon gluon PDF in a lattice-QCD calculation was done based on a quasi-PDF approach [31], but it did not obtain a sufficient signal to reconstruct the gluon PDF $g(x)$. Lattice calculations to access the nucleon, pion, and kaon gluon PDFs $g(x)$ followed [32–35] using the pseudo-PDF approach. However, the calculation of the gluon PDF via the pseudo-PDF method gives the ratio of $xg(x)/\langle x \rangle_g$, and one still needs a direct lattice calculation of $\langle x \rangle_g$ to extract

the gluon PDF by itself. Therefore, the lattice gluon momentum fraction remains an important input in the era of x -dependent PDF lattice hadronic calculations.

In this work, we present a lattice-QCD calculation of gluon momentum fraction $\langle x \rangle_g$ in the physical-continuum limit using clover fermions on $N_f = 2 + 1 + 1$ HISQ lattices with three lattice spacings, 0.09, 0.12, and 0.15 fm, and three pion masses, 690, 310, and 220 MeV. The rest of the paper is organized as follows. In Sec. II, we present the lattice setup and examples of how we extract the ground-state matrix elements from the lattice correlators to obtain the bare gluon momentum fraction of the nucleon. In Sec. III, the method and results of the nonperturbative renormalization of the gluon momentum fraction are discussed. In Sec. IV, we extrapolate the renormalized gluon momentum fractions of different ensembles to the physical pion mass and continuum limit then compare our results with other lattice calculations and global fits. We discuss possible systematics that may contribute to additional uncertainties in our results. A summary and the outlook for future calculations of the nucleon gluon momentum fraction can be found in Sec. V.

II. LATTICE SETUP AND BARE GLUON MATRIX ELEMENTS

We present our calculation of the nucleon gluon PDFs using clover valence fermions on four ensembles with $N_f = 2 + 1 + 1$ highly improved staggered quarks (HISQ) [36] generated by the MILC Collaboration [37] with three different lattice spacings ($a \approx 0.9, 0.12, \text{ and } 0.15$ fm) and three pion masses (220, 310, and 690 MeV),

TABLE II. Lattice spacing a , valence pion mass M_π^{val} and η_s mass $M_{\eta_s}^{\text{val}}$, lattice size $L^3 \times T$, number of configurations N_{cfg} , number of total two-point correlator measurements $N_{\text{meas}}^{2\text{pt}}$, and source-sink separation t_{sep} used in the three-point correlator fits of $N_f = 2 + 1 + 1$ clover valence fermions on HISQ ensembles generated by the MILC Collaboration and analyzed in this study.

Ensemble	a09m310	a12m220	a12m310	a15m310
a (fm)	0.0888(8)	0.1184(10)	0.1207(11)	0.1510(20)
$L^3 \times T$	$32^3 \times 96$	$32^3 \times 64$	$24^3 \times 64$	$16^3 \times 48$
M_π^{val} (MeV)	313.1(13)	226.6(3)	309.0(11)	319.1(31)
$M_{\eta_s}^{\text{val}}$ (MeV)	698.0(7)	N/A	684.1(6)	687.3(13)
N_{cfg}	1009	957	1013	900
N_{meas}	387,456	1,466,944	324,160	259,200
t_{sep}	[8,12]	[7,11]	[7,11]	[5,9]

as shown in Table II. The masses of the clover quarks are tuned to reproduce the lightest light and strange sea pseudoscalar meson masses done by the PNDME Collaboration [38–41]. PNDME calculated the nucleon quark isovector, helicity, and transversity moments using the clover-on-HISQ ensembles (“mixed action”) in Ref. [42]; the quark momentum fraction results obtained in Ref. [42] are consistent with the phenomenological global-fit values. In this work, we use five HYP-smearing [43] steps on the gluon loops to reduce the statistical uncertainties, based on the study in Ref. [31]. Table II shows the ensemble information, such as the lattice size $L^3 \times T$ and number of total two-point correlator measurements N_{meas} in this calculation. The number of measurements varies 10^5 – 10^6 for different ensembles.

On the lattice, we calculate the two-point correlator for a nucleon N via

$$C_N^{2\text{pt}}(P_z; t) = \langle 0 | \Gamma \int d^3y e^{-iy_z P_z} \chi(\vec{y}, t) \chi(\vec{0}, 0) | 0 \rangle, \quad (2)$$

where P_z is the boosted nucleon momentum along the spatial z direction, t is lattice Euclidean time, $\chi(y) = \epsilon^{lmn} [u(y)^T i\gamma_4 \gamma_2 \gamma_5 d^m(y)] u^n(y)$ [where $\{l, m, n\}$ are color indices, $u(y)$ and $d(y)$ are the quark operators] is the nucleon interpolation operator, and $\Gamma = \frac{1}{2}(1 + \gamma_4)$ is the projection operator. To minimize the autocorrelations of observables on these ensembles, we use random source locations at each time slice. We check each ensemble to see how the correlators vary for $N_{\text{bin}} \in [1, 10]$ and found the variation to show signs of small autocorrelations. We also calculate the three-point correlator to obtain the matrix elements needed to extract the gluon momentum fraction via

$$C_N^{3\text{pt}}(P_z; t_{\text{sep}}, t) = \int d^3y e^{-iy_z P_z} \langle \chi(\vec{y}, t_{\text{sep}}) | O_{g,\mu}(t) | \chi(\vec{0}, 0) \rangle, \quad (3)$$

where t_{sep} is the source-sink separation and t is the gluon-operator insertion time. The operator for the gluon momentum fraction $O_{g,\mu}(t)$ is

$$O_{g,\mu\nu} \equiv \sum_{i=x,y,z,t} F^{\mu i} F^{\nu i} - \frac{1}{4} \sum_{i,j=x,y,z,t} F^{ij} F^{ij}, \quad (4)$$

where the field tensor $F_{\mu\nu}$ is

$$F_{\mu\nu} = \frac{i}{8a^2 g} (\mathcal{P}_{[\mu,\nu]} + \mathcal{P}_{[\nu,-\mu]} + \mathcal{P}_{[-\mu,-\nu]} + \mathcal{P}_{[-\nu,\mu]}), \quad (5)$$

with the plaquette $\mathcal{P}_{\mu,\nu} = U_\mu(x) U_\nu(x + a\hat{\mu}) U_\mu^\dagger(x + a\hat{\nu}) U_\nu^\dagger(x)$ and $\mathcal{P}_{[\mu,\nu]} = \mathcal{P}_{\mu,\nu} - \mathcal{P}_{\nu,\mu}$. The same gluon operator was also used in the recent calculation of the gluon momentum fraction by the χ QCD, ETMC, and MIT Lattice Collaborations [21–26].

Using the two- and three-point correlators, we can extract the ground-state nucleon matrix elements that lead to the gluon momentum fraction. We use Gaussian momentum smearing for the quark fields [44] $q(x) + \alpha \sum_j U_j(x) e^{i(\frac{2\pi}{L}) \mathbf{k} \cdot \hat{e}_j} q(x + \hat{e}_j)$, so that we can calculate the momentum fraction using $P_z \neq 0$; these correlators have been neglected in previous calculations due to their worse signal-to-noise ratios relative to those obtained from $P_z = 0$. We fit the two-point and three-point correlators to the energy-eigenstate expansion,

$$C_N^{2\text{pt}}(P_z; t) = |A_{N,0}| e^{-E_{N,0}t} + |A_{N,1}| e^{-E_{N,1}t} + \dots, \quad (6)$$

$$C_N^{3\text{pt}}(z, P_z; t_{\text{sep}}, t) = |A_{N,0}|^2 \langle 0 | O_{g,\mu} | 0 \rangle e^{-E_{N,0}t_{\text{sep}}} + |A_{N,0}| |A_{N,1}| \langle 0 | \mathcal{O} | 1 \rangle e^{-E_{N,1}(t_{\text{sep}}-t)} e^{-E_{N,0}t} + |A_{N,0}| |A_{N,1}| \langle 1 | \mathcal{O} | 0 \rangle e^{-E_{N,0}(t_{\text{sep}}-t)} e^{-E_{N,1}t} + |A_{N,1}|^2 \langle 1 | \mathcal{O} | 1 \rangle e^{-E_{N,1}t_{\text{sep}}} + \dots, \quad (7)$$

where the ground (first-excited) state amplitudes and energies $A_{N,0}$, $E_{N,0}$ ($A_{N,1}$, $E_{N,1}$) are obtained from the two-state fits of the two-point correlators. The parameters $\langle 0 | \mathcal{O} | 0 \rangle$, $\langle 0 | \mathcal{O} | 1 \rangle$ ($\langle 1 | \mathcal{O} | 0 \rangle = \langle 0 | \mathcal{O} | 1 \rangle^*$), and $\langle 1 | \mathcal{O} | 1 \rangle$ are the ground-state, the ground-excited-state, and the excited-state matrix elements, respectively. The matrix elements can be extracted by using the two-state simultaneous fits (“two-sim fits”) of the three-point correlators using multiple t_{sep} inputs.

To visualize the quality of our fitted matrix-element extraction, we use ratios composed of the three-point ($C_N^{3\text{pt}}$) to the two-point ($C_N^{2\text{pt}}$) correlator, R_N^{Ratio} , defined as

$$R_N^{\text{Ratio}}(P_z; t_{\text{sep}}, t) = \frac{C_N^{3\text{pt}}(P_z; t_{\text{sep}}, t)}{C_N^{2\text{pt}}(P_z; t_{\text{sep}})}; \quad (8)$$

if the excited-state contamination were small, we would see the midpoints of $t - t_{\text{sep}}/2$ approach the true ground state,

and these values would be independent of the t_{sep} . Figures 1 and 2 show the bare matrix element extracted at $P_z = 2$ lattice units ($2\pi P_z/(aL)$ in physical units) from three-point and two-point correlators of strange- and light-quark nucleons, respectively, for all four ensembles studied in this paper. The leftmost column of the figures shows the fitted ground-state gluon matrix elements $\langle 0|\mathcal{O}|0\rangle$ (grey band) with multiple source-sink separations of R^{Ratio} (red to purple points) and the reconstruction of the fits to the ratio plots (red to purple bands). We found that the R^{Ratio} has a tendency to increase with larger source-sink separation t_{sep}

and toward the ground-state matrix elements obtained from the “two-sim” fit in Eq. (7) (the grey band). The second column of Figs. 1 and 2 shows two-sim fits by fixing $t_{\text{sep}}^{\text{max}}$ at 12, 11, 11, and 9 for the a09m310, a12m220, a12m310, and a15m310 ensembles, respectively, while varying the $t_{\text{sep}}^{\text{min}}$. We found that our ground-state matrix elements are consistent among different choices of $t_{\text{sep}}^{\text{min}}$. Similarly, we check the dependence on $t_{\text{sep}}^{\text{max}}$ by fixing $t_{\text{sep}}^{\text{min}}$ of two-sim fits at 8, 7, 7, and 5 for the a09m310, a12m220, a12m310, and a15m310 ensembles, respectively. The ground-state matrix elements are mostly consistent with different choices $t_{\text{sep}}^{\text{max}}$.

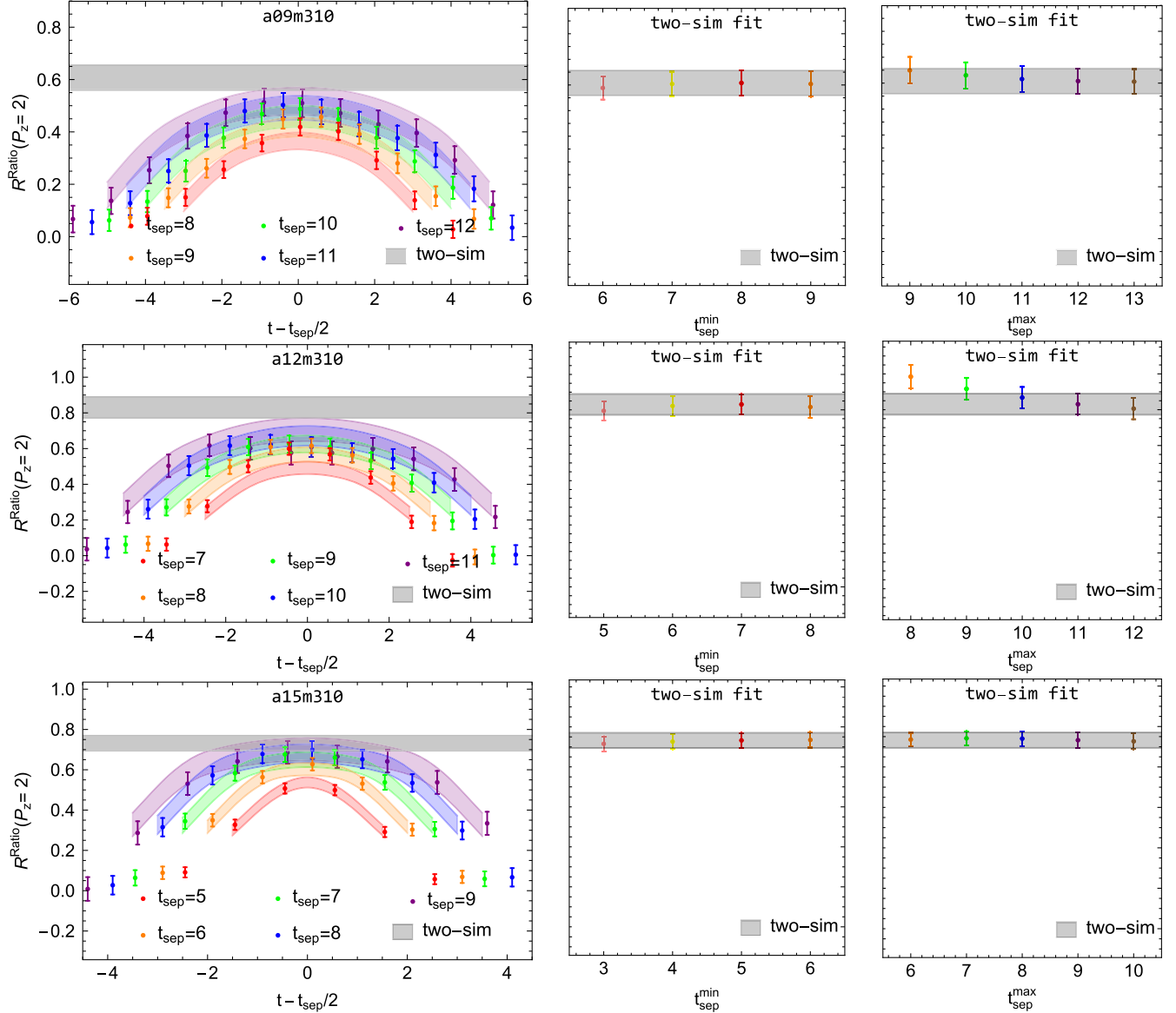


FIG. 1. Example ratio plots (left), two-sim fits (right two columns) from the a09m310, a12m310, and a15m310 ensembles (from top to bottom) with pion mass $M_\pi \approx 690$ MeV, respectively. The gray bands show the extracted ground-state matrix element $\langle 0|\mathcal{O}|0\rangle$ obtained from a two-sim fit using $t_{\text{sep}} \in [8, 12]$, $[7, 11]$ and $[5, 9]$ for the a09m310, a12m310, and a15m310 ensembles, respectively. The first column shows the ratio of the three-point to two-point correlators with the reconstructed fit bands from the two-sim fit, shown as functions of $t - t_{\text{sep}}/2$. The second (third) column shows the two-sim ground-state matrix element $\langle 0|\mathcal{O}|0\rangle$ results with fixed $t_{\text{sep}}^{\text{max}}$ ($t_{\text{sep}}^{\text{min}}$) inputs as shown in Table II while varying $t_{\text{sep}}^{\text{min}}$ ($t_{\text{sep}}^{\text{max}}$) to see how stable the ground-state matrix elements are.

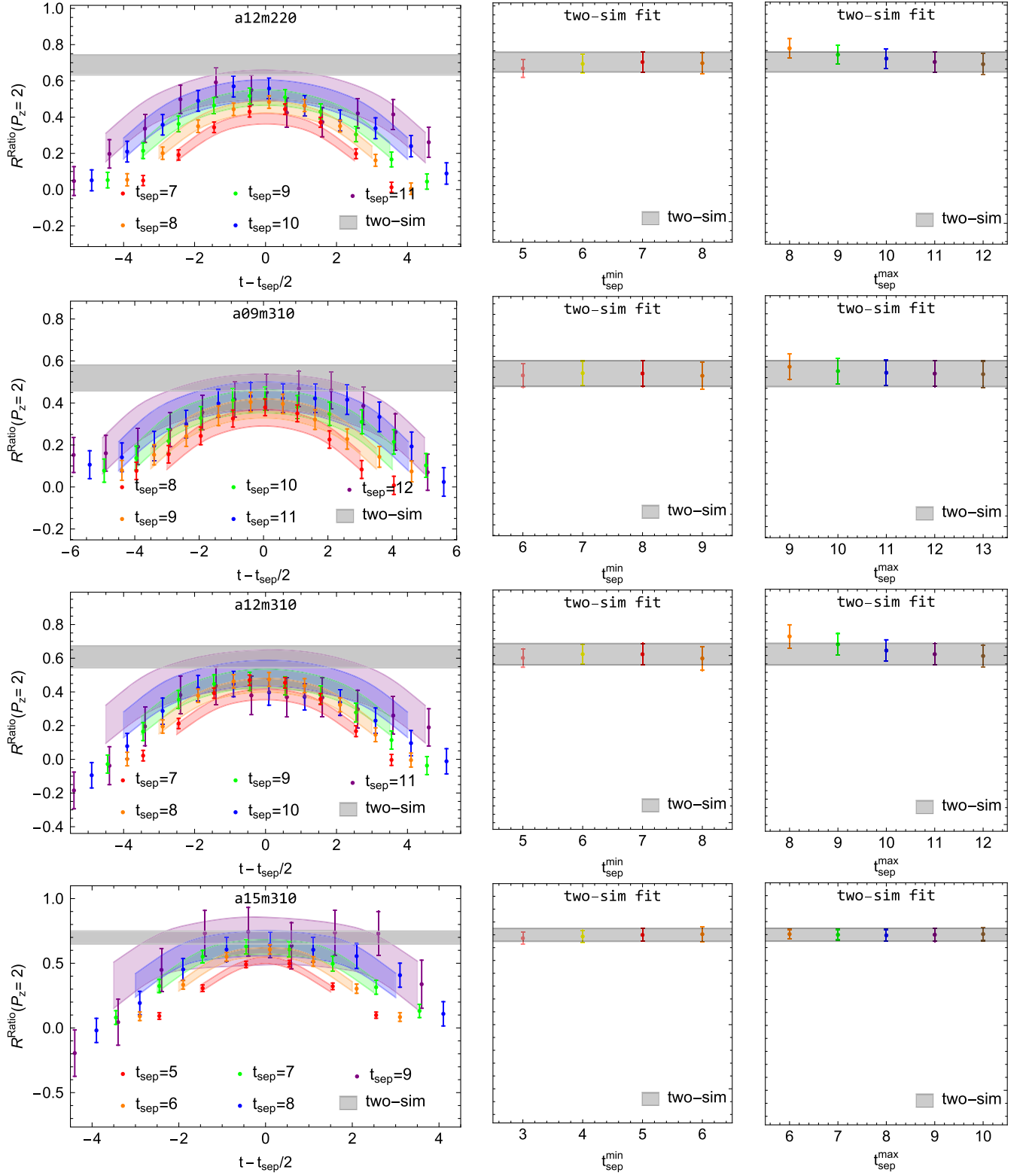


FIG. 2. Example ratio plots (left-most column), and two-sim fits (right 2 columns) from the a12m220, a09m310, a12m310, a15m310 ensembles (from top to bottom) with pion masses $M_\pi \approx \{220, 310, 310, 310\}$ MeV, respectively. The gray bands show the extracted ground-state matrix element $\langle 0|\mathcal{O}|0\rangle$ obtained from the two-sim fit using the $t_{\text{sep}} \in [7, 11]$, $[8, 12]$, $[7, 11]$, and $[5, 9]$ for the a12m220, a09m310, a12m310, and a15m310 ensembles, respectively. The first column shows the ratio of the three-point to two-point correlators with the reconstructed fit bands from the two-sim fit, shown as functions of $t - t_{\text{sep}}/2$. The second (third) column shows the two-sim ground-state matrix element $\langle 0|\mathcal{O}|0\rangle$ results with fixed $t_{\text{sep}}^{\text{min}}$ ($t_{\text{sep}}^{\text{max}}$) inputs as shown in Table II while varying $t_{\text{sep}}^{\text{max}}$ ($t_{\text{sep}}^{\text{min}}$) to see how stable the ground-state matrix elements are.

Based on the above procedure, we choose the final source-sink separation t_{sep} (listed in Table II in lattice units) used in the “two-sim” fits for the rest of this work.

The majority of our two-sim fits to the three-point correlators using the parameters listed in Table II have reasonable fits with $\chi^2/\text{d.o.f.} < 1$. The 690-MeV a12m310 nucleon matrix elements suffer from slightly worse fits with $\chi^2/\text{d.o.f.} \approx 1.7$. We have varied the parameters without much improvement in the quality of fit; however, the obtained matrix elements remain consistent as long as $t_{\text{sep}}^{\text{max}} > 8$. In later sections, we will see the impact of these two matrix elements in the continuum-physical extrapolation.

We repeat the same analysis routine for $P_z \in [0, 4] \frac{2\pi}{L} a^{-1}$ to take advantage of the momentum-averaged results. The above bare ground-state matrix elements $\langle 0|\mathcal{O}|0\rangle$ obtained from two-sim fits in Eq. (7) contain a kinematic factor

$\frac{E_0}{\frac{3}{4}E_0^2 + \frac{1}{4}P_z^2}$. After dividing out this kinematic factor, we obtain the bare gluon momentum fraction $\langle x \rangle_g^{\text{bare}}$ (orange points) for four ensembles and various boost momenta, as shown in Figs. 3 and 4 for strange- and light-quark nucleons. We then

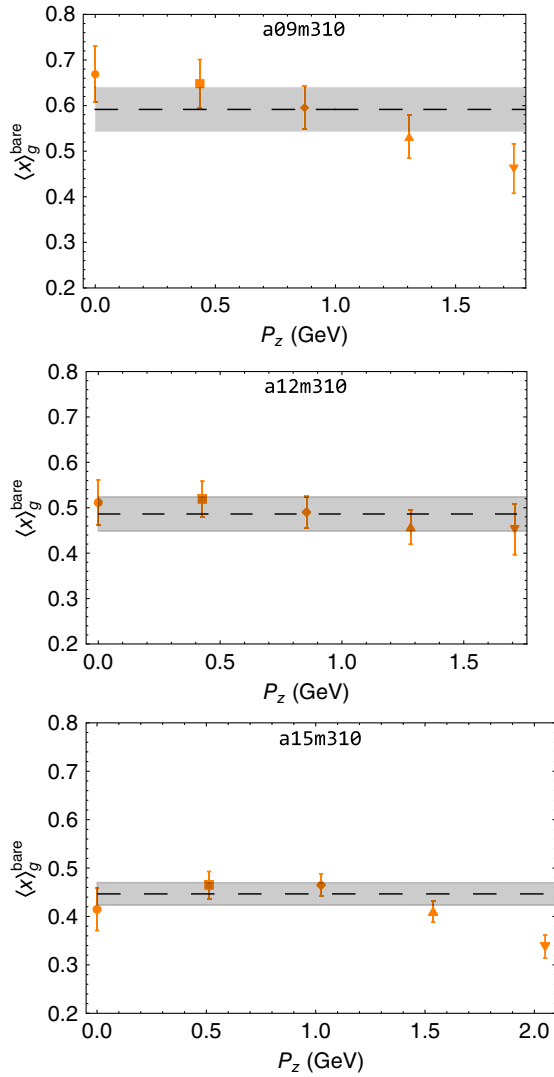


FIG. 3. The bare gluon momentum fraction $\langle x \rangle_g^{\text{bare}}$ and fitted bands divided by kinematic factors as functions of momentum $P_z = 2\pi \times N_z / (aL)$ for $M_\pi \approx 690$ MeV on a09m310, a12m310, and a15m310 ensembles, respectively.

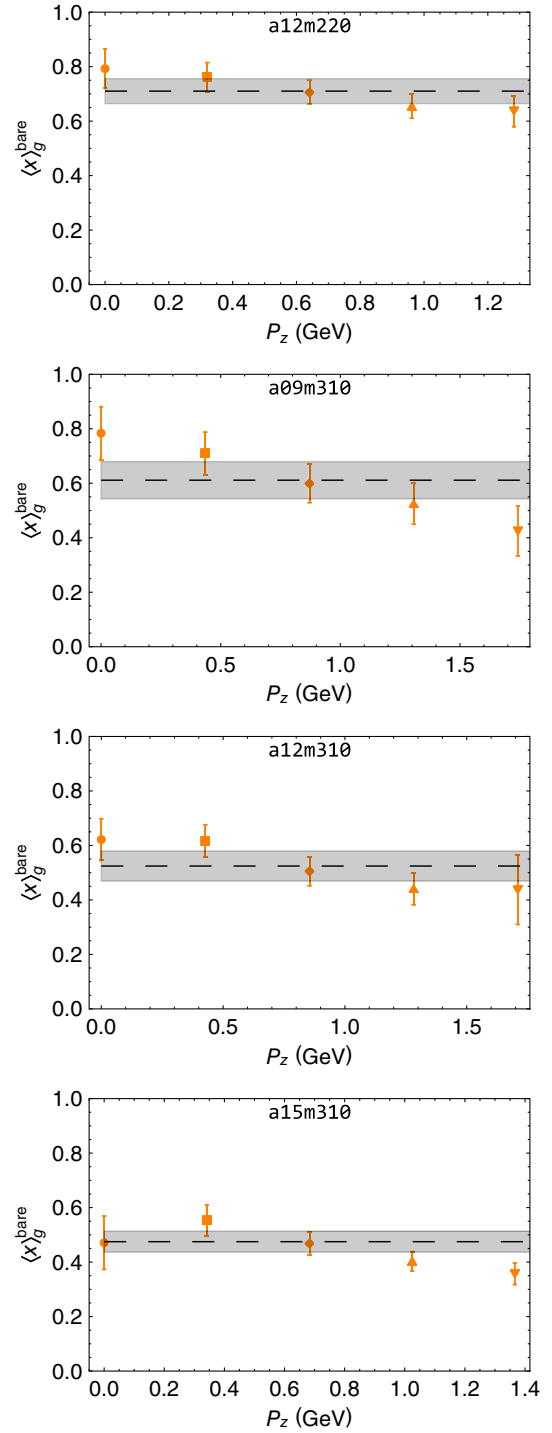


FIG. 4. The bare gluon momentum fraction $\langle x \rangle_g^{\text{bare}}$ and fitted bands dividing by kinematic factors as functions of momentum $P_z = 2\pi \times N_z / (aL)$ for $M_\pi \approx \{220, 310, 310, 310\}$ MeV on a12m220, a09m310, a12m310, and a15m310 ensembles, respectively.

TABLE III. The renormalization constant $(Z_{O_g}^{\overline{\text{MS}}})^{-1}$, the bare gluon momentum fraction $\langle x \rangle_g^{\text{bare}}$, and the renormalized gluon momentum fraction $\langle x \rangle_g^{\overline{\text{MS}}}$ for the four ensembles used in this calculation. We use the a12m310 NPR factors for a12m220 $\langle x \rangle_g^{\overline{\text{MS}}}$ calculation since the mass dependence is weak for the NPR factors. In the final column, the first error is the statistical error from the matrix element and the second error is due to the NPR factor.

Ensemble	M_π^{val} (MeV)	$\langle x \rangle_g^{\text{bare}}$	$(Z_{O_g}^{\overline{\text{MS}}})^{-1}$	$\langle x \rangle_g^{\overline{\text{MS}}}$
a12m220	226.6(3)	0.710(45)	1.512(65)	0.470(30)(25)
a09m310	313.1(13)	0.622(63)	1.336(106)	0.466(46)(37)
	698.0(7)	0.592(48)	1.336(106)	0.443(37)(35)
a12m310	309.0(11)	0.651(53)	1.512(65)	0.430(35)(19)
	684.1(6)	0.637(41)	1.512(65)	0.421(27)(18)
a15m310	319.1(31)	0.475(38)	1.024(61)	0.464(37)(27)
	687.3(13)	0.447(23)	1.024(61)	0.436(22)(26)

fit the bare matrix elements of $P_z \in [0, 4] \times 2\pi/(aL)$ on each ensemble to a constant, shown as a gray band in the figures. The $\chi^2/\text{d.o.f.}$ of the fits are smaller than 1.5 except the a09m310 light nucleon fit, which is the noisiest dataset and has $\chi^2/\text{d.o.f.} \approx 1.7$. The final bare gluon momentum fractions are listed in Table III.

III. NONPERTURBATIVELY RENORMALIZED GLUON MOMENTUM FRACTION

After we determine the gluon bare momentum fraction matrix element from lattice calculation, our next step is to renormalize it. In this work, we will be using RI-MOM-scheme NPR [45]. We then implement a perturbative matching to convert the gluon momentum fraction into the $\overline{\text{MS}}$ scheme as follows:

$$\begin{aligned} \langle x \rangle_g^{\overline{\text{MS}}} &= Z_{O_g}^{\overline{\text{MS}}}(\mu^2, \mu_R^2) \langle x \rangle_g^{\text{bare}} \\ &= R^{\overline{\text{MS}}}(\mu^2, \mu_R^2) Z_{O_g}^{\text{RI}}(\mu_R^2) \langle x \rangle_g^{\text{bare}}, \end{aligned} \quad (9)$$

where $Z_{O_g}^{\overline{\text{MS}}}(\mu^2, \mu_R^2)$ is the renormalization constant, and the one-loop expression for the perturbative matching ratio $R^{\overline{\text{MS}}}(\mu^2, \mu_R^2)$, derived in Ref. [46], is

$$\begin{aligned} R^{\overline{\text{MS}}}(\mu^2, \mu_R^2) &= 1 - \frac{g^2 N_f}{16\pi^2} \left(\frac{2}{3} \log(\mu^2/\mu_R^2) + \frac{10}{9} \right) \\ &\quad - \frac{g^2 N_c}{16\pi^2} \left(\frac{4}{3} - 2\xi + \frac{\xi^2}{4} \right), \end{aligned} \quad (10)$$

where the number of flavors $N_f = 4$, the number of colors $N_c = 3$, the parameter from the Riemann zeta function $\xi = 0$ in the Landau gauge, g^2 is $4\pi\alpha(\mu)$ [47–49], and $\mu = 2 \text{ GeV}$ are used in our calculation. The RI-MOM renormalization factor $Z_{O_g}^{\text{RI}}(\mu_R^2)$ can be obtained with the condition,

$$Z_g(p^2) Z_{O_g}^{\text{RI}}(p^2) \Lambda_{O_g}^{\text{bare}}(p) (\Lambda_{O_g}^{\text{tree}}(p))^{-1} \Big|_{p^2=\mu_R^2} = 1, \quad (11)$$

where $Z_g(p^2)$ is the gluon-field renormalization and $\Lambda_{O_g}^{\text{bare (tree)}}$ is the bare (tree-level) amputated Green function for the operator O_g in the Landau-gauge-fixed gluon state. The NPR factor $Z_{O_g}^{\text{RI}}(p^2)$ of the operator in Eq. (4) is derived in Refs. [23,24],

$$\begin{aligned} &(Z_{O_g}^{\text{RI}})^{-1}(\mu_R^2) \\ &= \frac{p^2 \langle (O_{g,\mu\mu} - O_{g,\nu\nu}) \text{Tr}[A_\tau(p)A_\tau(-p)] \rangle}{2(p_\mu^2 - p_\nu^2) D_{g,\tau\tau}(p)} \Big|_{p^2=\mu_R^2, \tau \neq \mu \neq \nu, p_\tau=0} \end{aligned} \quad (12)$$

Therefore, the gluon propagator $D_{g,\mu\nu}(p)$ and bare gluon amputated Green function $\Lambda_{O_g}^{\text{bare}}(p)$ need to be calculated for the further calculation of the NPR factor,

$$\begin{aligned} D_{g,\mu\nu}(p) &= \langle \text{Tr}[A_\mu(p)A_\nu(-p)] \rangle \\ \Lambda_{O_g}^{\text{bare}}(p) &= \frac{\langle (O_{g,\mu\mu} - O_{g,\nu\nu}) \text{Tr}[A_\tau(p)A_\tau(-p)] \rangle (N_c^2 - 1)^2}{4D_{g,\tau\tau}^2(p)}, \end{aligned} \quad (13)$$

where $\tau, \mu, \nu \in \{x, y, z, t\}$ and $\tau \neq \mu \neq \nu$. Following the above procedure, $Z_{O_g}^{\overline{\text{MS}}}(\mu^2 = 4 \text{ GeV}^2, p^2)$ is calculated and shown in Fig. 5 in light gray points by using the full lattice of all ensembles listed in Table II. The signal-to-noise ratios of the light gray points are smaller than 100% in most cases, which gives us a useless renormalized gluon momentum fraction. The relative errors also become larger as the lattice spacing becomes smaller. For example, the relative errors of $Z_{O_g}^{\overline{\text{MS}}}(\mu^2 = 4 \text{ GeV}^2, p^2)$ for a09m310 ensemble are ≈ 1.5 on 347 configurations. To achieve a comparable relative error as the bare matrix elements of the light nucleon (0.10) shown in Table III, we need $15^2 \times 347 = 78,075$ configurations for the a09m310 NPR calculation alone, which is very expensive to do in dynamical gauge generation. Therefore, we need some technique to reduce the error of the NPR factor without requiring a huge number of configurations in the calculation.

In Refs. [24,50], χQCD introduces a technique called cluster-decomposition error reduction (CDER) in order to increase the signal-to-noise ratio of NPR factor, which has not been widely used by other lattice groups. The reason for such error reduction is that, for the operator insertions, the correlator signal falls off exponentially with the distance, while the error remains constant. Beyond a certain correlation length, it will only increase the noise without gaining any signal. χQCD introduced two additional cutoffs in the CDER technique [24] for calculating the gluon NPR: r_1 (r_2) for the upper bound of the distance between the glue operator and one of the gauge fields (the gauge fields in the gluon propagator $D_g(p)$) in the gluon amputated Green

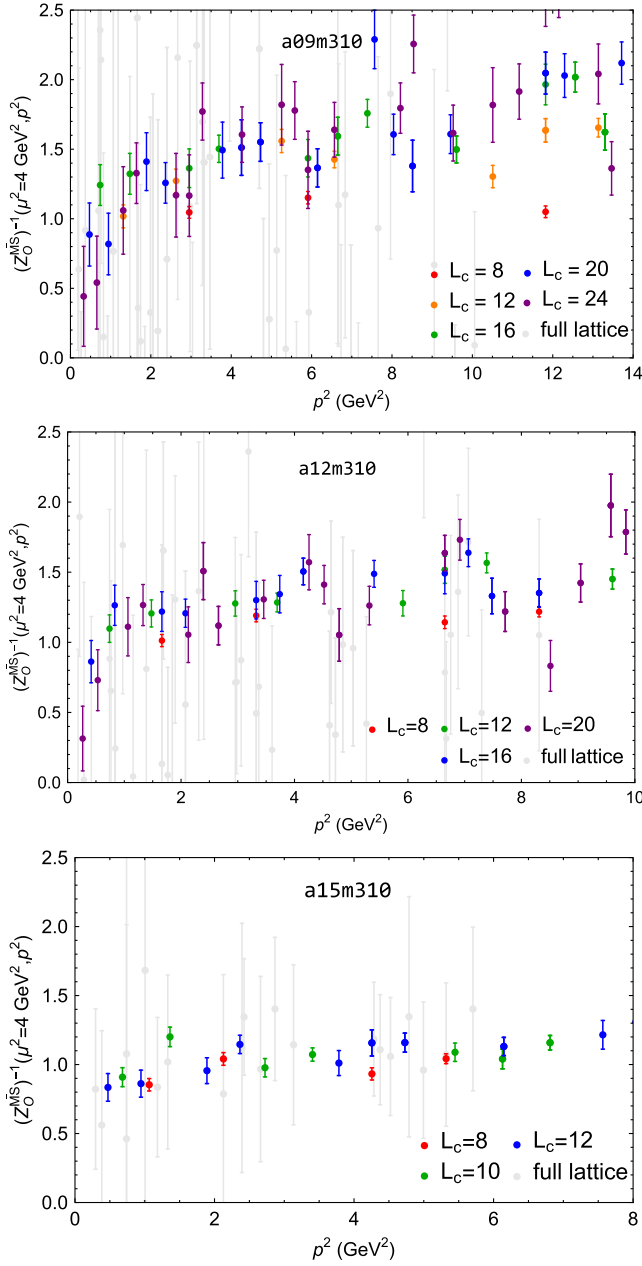


FIG. 5. The renormalization constants $(Z_{O_g}^{\overline{\text{MS}}})^{-1}(\mu = 4 \text{ GeV}^2, p^2)$ as a function of $p^2(\text{GeV}^2)$ for the a09m310, a12m310, and a15m310 ensembles are shown in the first second, and last rows, respectively. Different color points represent different cutoffs L_c and the lighter gray large error bar points are from the full lattice calculations.

function $\Lambda_{O_g}(p)$ definition. With these two cutoffs, the correlators in the gluon propagator and gluon amputated Green function become

$$\begin{aligned} & \langle \text{Tr}[A_\mu(p)A_\nu(-p)] \rangle \\ & \approx \left\langle \int_{|r|<r_2} d^4 r' \int d^4 x e^{ip \cdot r'} \text{Tr}[A_\mu(x)A_\nu(x+r')] \right\rangle, \quad (14) \end{aligned}$$

$$\begin{aligned} & \langle (O_{g,\mu\mu} - O_{g,\nu\nu}) \text{Tr}[A_\tau(p)A_\tau(-p)] \rangle \\ & \approx \left\langle \int_{|r|<r_1} d^4 r \int_{|r'|<r_2} d^4 r' \int d^4 x e^{ip \cdot r'} \right. \\ & \quad \left. \times [O_{g,\mu\mu} - O_{g,\nu\nu}](x+r) \text{Tr}[A_\tau(x)A_\tau(x+r')] \right\rangle. \quad (15) \end{aligned}$$

Reference [24] studies the gluon nonperturbative renormalization on different types of gauge configurations: 2 + 1-flavor RBC/UKQCD domain-wall fermion (DWF) with lattice spacing $a = 0.114 \text{ fm}$, $m_\pi = 140 \text{ MeV}$, a quenched Wilson gauge ensemble of 0.098 fm , and two volumes of 0.117 fm 450-MeV two-flavor clover fermion as well. In their quenched and two-flavor clover fermion studies, they compare the NPR-factor $Z_{O_g}^{\text{RI}}$ results using the CDER technique and $100\times$ statistics and show that they are consistent within one sigma. They find that the CDER technique provides improvements on the lattice with their final choices of $r_1 \approx 0.9 \text{ fm}$ and $r_2 \approx 1.3 \text{ fm}$, and such improvements are insensitive to the lattice definition of operators and the HYP smearing steps within their uncertainties. In our work, instead of using the CDER radius cutoffs from Ref. [51], we use 16 L_c^4 truncated lattices to calculate the NPR factor $Z_{O_g}^{\overline{\text{MS}}}(\mu^2, \mu_R^2)$ for each lattice spacing, which means using a 4-D cubic cutoff instead of a spherical cutoff and $L_c \approx 2r_1$ and $2r_2$. The details of the number of measurements for each lattice spacing and L_c can be found in Table IV.

The smallest cutoffs L_c we use are 8 lattice units, which correspond to 0.72, 0.96, and 1.2 fm for the a09m310, a12m310, and a15m310 ensembles, respectively; this corresponds to $2r_1$ with similar smallest cutoff $\approx 0.8 \text{ fm}$ used in Ref. [24]. Figure 5 shows the $(Z_{O_g}^{\overline{\text{MS}}}(\mu^2 = 4 \text{ GeV}^2, p^2))^{-1}$ as a function of p^2 for different cutoffs L_c for three ensembles (also the full lattices in grey points). The error of $Z_{O_g}^{\overline{\text{MS}}}(\mu^2 = 4 \text{ GeV}^2, p^2)$ becomes smaller as L_c decreases, which is expected as per the χ QCD results [24]. Different L_c results are consistent within a one sigma error range except for the $L_c = 8$ in a09m310 ensemble, likely suffering from finite-volume effects. Our final choice of the cutoffs are $L_c = \{1.44, 1.44, 1.5\} \text{ fm}$ for a09m310, a12m310, and a15m310 ensembles, respectively, where L is the full lattice size. These cutoff lengths of

TABLE IV. The truncation length L_c in lattice units and the number of configurations N_{cfg} and measurements N_{meas} used for different lattice-spacing ensembles. We used 16 sources for the truncation on each configuration; thus, N_{meas} is $16 \times N_{\text{cfg}}$.

Ensemble	a09m310	a12m310	a15m310
L_c	{8, 12, 16, 20, 24}	{8, 12, 16, 20}	{8, 10, 12}
N_{cfg}	347	409	394
N_{meas}	5552	6544	6304

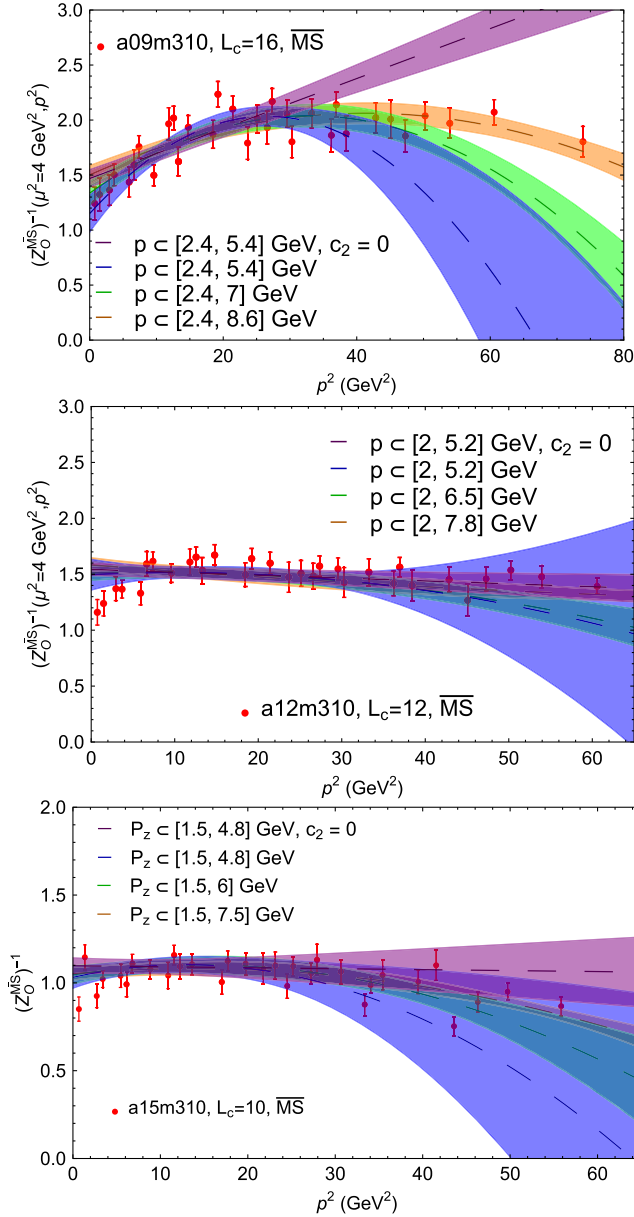


FIG. 6. The renormalization constants $(Z_{O_g}^{\overline{MS}})^{-1}(\mu^2=4\text{ GeV}^2, p^2)$ as a function of p^2 for the a09m310 $L_c = 16$, a12m310 $L_c = 12$, and a15m310 $L_c = 8$ with various fit momentum ranges are shown from top to bottom, respectively. The lower limits of the fit range of the momentum are chosen to be the same as in Ref. [42].

$L_c \in [1.44, 1.5]$ fm which correspond to $r_1 \approx 0.7$ fm are shown to be consistent with the full lattice NPR factors in the χ QCD work [24].

We fit the p^2 -dependent renormalization factor according to the form,

$$(Z_{O_g}^{\overline{MS}})^{-1}(\mu^2 = 4 \text{ GeV}^2, p^2) = (Z_{O_g}^{\overline{MS}})^{-1} + c_1 p^2 + c_2 p^4, \quad (16)$$

where $(Z_{O_g}^{\overline{MS}})^{-1}$ on the right-hand side of the equation is the renormalization factor at $\mu^2 = 4 \text{ GeV}^2$ and $p^2 = 0$. Figure 6 shows examples with our choice of L_c for all three lattice spacings and the corresponding fit bands using Eq. (16) with ($c_2 \neq 0$) and without ($c_2 = 0$) the quadratic term for large and small p^2 ranges used in the fit. We only use p larger than 1.5, 2.0, and 2.4 GeV for $a \approx 0.15, 0.12$, and 0.09 fm, respectively, based on the p_{\min} used in quark momentum fractions on the same mixed-action study by PNDME [42]. (PNDME only used constant fits to determine the renormalization constants.) For the largest lattice spacing (a15m310 ensemble), the renormalization constants $(Z_{O_g}^{\overline{MS}})^{-1}(\mu^2 = 4 \text{ GeV}^2, p^2)$ are quite linear as a function of p^2 . Therefore, different fit bands are consistent for different fit ranges of p^2 with ($c_2 \neq 0$) and without the ($c_2 = 0$) the quadratic term. The fit bands of $(Z_{O_g}^{\overline{MS}})^{-1}(\mu^2 = 4 \text{ GeV}^2, p^2)$ of the a12m310 ensemble are still consistent with each other within the one-sigma error despite the large error for the smallest p^2 range $p \in [2, 5.2]$ GeV. The fit bands of $(Z_{O_g}^{\overline{MS}})^{-1}(\mu^2 = 4 \text{ GeV}^2, p^2)$ of the a12m310 ensemble deviate at large p^2 , because the $(Z_{O_g}^{\overline{MS}})^{-1}(\mu^2 = 4 \text{ GeV}^2, p^2)$ points increase and then decrease from small to large p^2 , which shows that $(Z_{O_g}^{\overline{MS}})^{-1}(\mu^2 = 4 \text{ GeV}^2, p^2)$ is not so linear as a function of p^2 . Finally, the fit results of a09m310 $(Z_{O_g}^{\overline{MS}})^{-1}(\mu^2 = 4 \text{ GeV}^2, p^2)$ at $p^2 = 0$ start to converge at ranges with larger maximum p^2 chosen for the fit. Thus, we can choose $p \in [2.4, 7]$ GeV as the fit range for later calculations. To summarize, we use the quadratic fits with p ranges [1.5, 6], [2, 6.5], and [2.4, 7] GeV for each L_c to extract the renormalization constants. The renormalization constants $(Z_{O_g}^{\overline{MS}})^{-1}$ for the three ensembles are listed in Table III. Using Eq. (9), we obtain the renormalized gluon momentum fraction $\langle x \rangle_g^{\overline{MS}}$ results on four ensembles for both light and strange nucleons, listed in Table III.

IV. RESULTS AND DISCUSSION

Combining the results from Secs. II and III, we obtain renormalized gluon momentum fractions $\langle x \rangle_g^{\overline{MS}}$ at three lattice spacings and three pion masses as shown in Fig. 7. The points in Fig. 7 have two kinds of error bars; the darker smaller bars include only the statistical error for the gluon momentum fraction, while the lighter larger bars include both the statistical errors and the errors from the gluon NPR factor. Our renormalized $\langle x \rangle_g^{\overline{MS}}$ shows weak pion-mass and lattice-spacing dependence. Therefore, we use a simple quadratic ansatz for M_π and a in the physical-continuum extrapolation to the physical pion mass $M_\pi^{\text{phys}} = 135 \text{ MeV}$ and continuum limit $a = 0$,

$$\langle x \rangle_g^{\overline{\text{MS}}}(M_\pi, a) = \langle x \rangle_g^{\overline{\text{MS}},\text{cont}} + k_M(M_\pi^2 - (M_\pi^{\text{phys}})^2) + k_a a^2. \quad (17)$$

In the fits depending on M_π and a , both the statistical errors and the NPR errors are considered. With the a15m310, a12m310, and a09m310 ensembles, since we have the same number of measurements for both strange and light quarks, within each ensemble, we bootstrap the light and strange renormalized matrix elements in the same way to keep the correlations. Across different ensembles, the data are independent. The physical-continuum limit gluon momentum fraction $\langle x \rangle_g^{\overline{\text{MS}},\text{cont}}$ fit result is 0.502(53). The fitted parameters $k_M = -8.1(5.2) \times 10^{-5} \text{ GeV}^{-2}$ and $k_a = -0.034(31) \text{ fm}^{-2}$ are very small, consistent with zero within two sigma. The reconstructed fit bands at selected $M_\pi \in \{135, 310, 690\}$ MeV as functions of a are shown in the left plot of Fig. 7. There is a slight trend toward higher gluon momentum fractions as one approaches the physical pion mass. The $M_\pi = 690$ MeV band deviates from the other two bands, while the $M_\pi = 135$ and 310 MeV bands almost coincide. One can also see that the fit form well describes the data since these bands go through the $M_\pi = 220$ - and 310-MeV data points. On the right-hand side of Fig. 7, we show reconstructed results at $a \in \{0, 0.09, 0.12, 0.15\}$ fm as functions of M_π . Each color band representing different lattice spacings agrees well with the same-color data points. The central values of continuum extrapolation favor higher gluon momentum fractions but remain within one sigma of the bands from all three lattice spacings.

So far, we have been missing a systematic error associated with the mixing from the quark sector. The bare operator in Eq. (4) can mix with the singlet quark

operators O_q^{bare} and couple with the renormalized gluon operator via $O_g = Z_{gg} O_g^{\text{bare}} + Z_{gq} \sum_{i=u,d,s} O_{q,i}^{\text{bare}}$. The mixing for quark operators is expected to be small, based on past lattice works. The ETM Collaboration [21,22,25] used one-loop perturbative renormalization and estimated the mixing coefficients to be a fraction of their statistical errors. The effect of the mixing of the quark operator into the gluon operator is about 2%–10%, as shown in Ref. [21]. An MIT group also ignored the quark mixing because it is assumed to be smaller than the statistical uncertainties [23]. We conservatively estimate a 10% systematic error from quark mixing for this calculation; thus, our final $\langle x \rangle_g^{\overline{\text{MS}},\text{cont}}$ at physical pion mass and continuum limit is $0.502(53)_{\text{stat+NPR}}(50)_{\text{mixing}}$.

We compare our results with prior dynamical lattice work and global fits. As shown in Table I, the majority of nucleon gluon momentum fractions $\langle x \rangle_g$ from lattice dynamical calculations were done using a single lattice spacing. These results range from 0.4 to 0.55 for the most recent calculations (except the ETMC16 and ETMC17 results) and have statistical errors varying from 5%–20%. The χ QCD Collaboration studied the systematic errors from continuum extrapolation and assigned it a 10% relative error in Ref. [26] and a 5% relative error in their most recent paper [27]. Overall, we find good consistency with lattice determinations from the last four years. We summarize the dynamical lattice-QCD results extrapolated to or directly calculated at physical pion mass, along with the global-fit results since 2014, in Fig. 8. The lattice results currently are much larger than with those from global fits, with central values closer to 0.5, rather than around 0.4, where global fits prefer. Higher-precision lattice

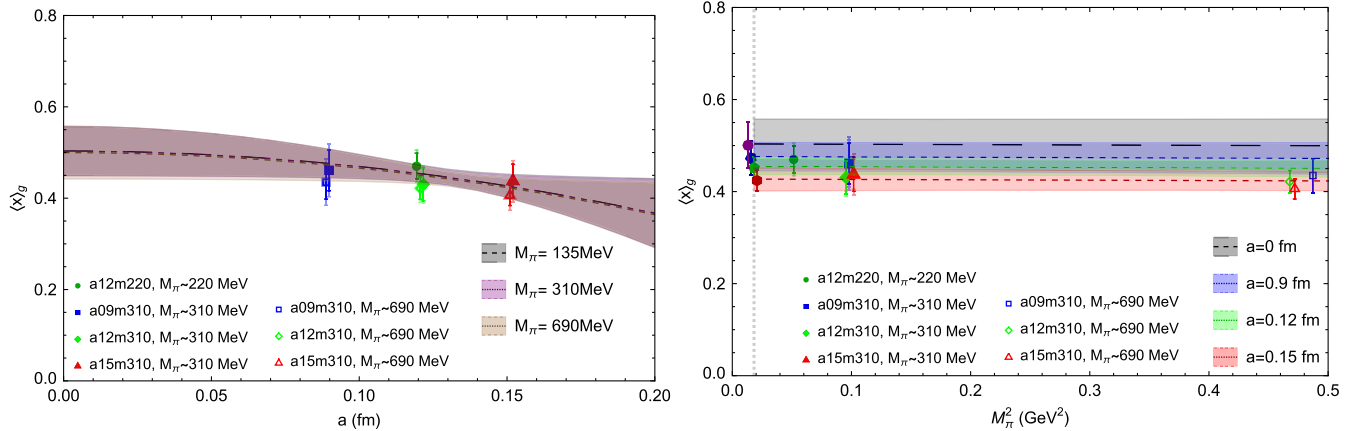


FIG. 7. The renormalized gluon momentum fraction $\langle x \rangle_g^{\overline{\text{MS}}}$ obtained from each ensemble along with the physical-continuum extrapolation as functions of lattice spacing a (left) and pion mass M_π^2 (right). Each data point in the plot has two errors: the darker inner bar indicates the statistical error, while the lighter outer bar includes combined errors from both the statistical and renormalization error. The vertical dashed line in the right plot goes through $M_\pi^2 = (0.135 \text{ GeV})^2$, and the different color points near this line represent the extrapolated values at different lattice spacings a at physical pion mass. To increase visibility, we plot the $M_\pi \in \{220, 310\}$ -MeV points shifted by +0.001 fm in the left plot. The reconstructed fit bands at selected $M_\pi \in \{135, 310, 690\}$ MeV as functions of a and at selected $a \in \{0, 0.09, 0.12, 0.15\}$ fm as functions of M_π are also shown in the left- and right-side plots, respectively.

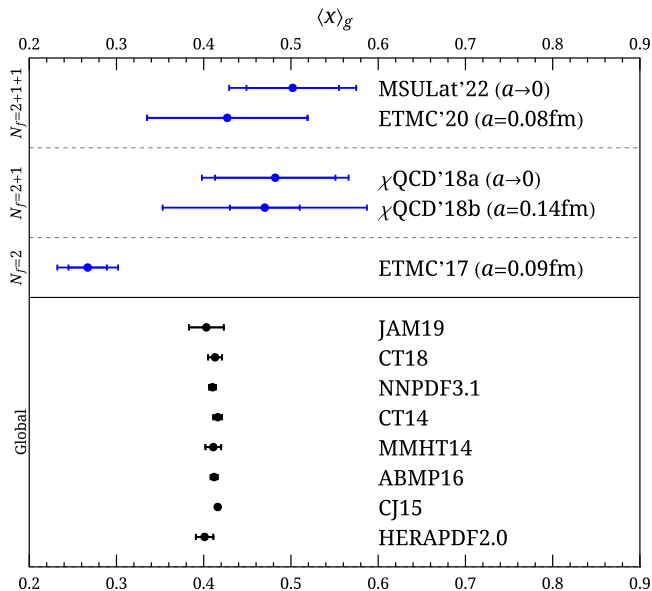


FIG. 8. Comparisons of lattice-QCD and global fit determinations of the gluon moments of unpolarized PDFs at $\mu = 2$ GeV. On the lattice side, we only show those results at or extrapolated to physical pion mass by this work (MSULat'22), ETMC'20 [25], χ QCD'18a [24], χ QCD'18b [26], and ETMC'17 [22], compared with global fit results from JAM19 [52], CT18 [53], NNPDF3.1 [3], CT14 [1], MMHT14 [2], ABMP16 [4], CJ15 [5], and HERAPDF2.0 [54] analyses. Some lattice-QCD calculations include systematic errors and some do not; we refer readers to Table 1 for more details on the difference in the errors. Overall, the lattice calculations prefer higher central values of the gluon momentum fraction than the global fits.

calculations are needed with order-of-magnitude increases in computational resources to reduce the errors to be comparable with those from global fits (using more than 60 years of experimental data).

V. CONCLUSION AND OUTLOOK

We present the first $N_f = 2 + 1 + 1$ continuum-limit lattice calculation of the gluon momentum fraction. We use high-statistics nucleon two-point correlators ranging from 0.26–1.5 million measurements with three lattice spacings and the lightest pion mass being 220 MeV. We apply a two-state fit to multiple source-sink separations to extract

ground-state matrix elements. We nonperturbatively calculate renormalization factors for these operators in the RI/MOM scheme, following the traditional NPR approach. For the ensembles at pion mass 310 MeV, even though the spatial volumes are roughly the same among our three lattice spacings, the finest lattice spacing, $a \approx 0.09$ fm, yields much noisier results. To improve this, we apply cluster-decomposition error reduction (CDER). The renormalized gluon momentum fractions show mild lattice-spacing and pion-mass dependence (within our statistical and NPR errors); thus, we use a simple ansatz to extrapolate to the physical-continuum limit. Our final gluon momentum fraction is $0.502(53)_{\text{stat+NPR}}(50)_{\text{mixing}}$, where the mixing systematic is estimated from upper bounds determined in previous lattice work. Our lattice results are consistent with lattice work from the last four years using single lattice spacings and $N_f = 2 + 1$ mixed action, and they are consistent with those from global fits within two sigma. Future calculations will include ensembles at the physical pion mass and lattice calculations of the quark moments.

ACKNOWLEDGMENTS

We thank the MILC Collaboration for sharing the lattices used to perform this study. The LQCD calculations were performed using the Chroma software suite [55]. This research used resources of the National Energy Research Scientific Computing Center, a DOE Office of Science User Facility supported by the Office of Science of the U.S. Department of Energy under Contract No. DE-AC02-05CH11231 through ERCAP; facilities of the USQCD Collaboration are funded by the Office of Science of the U.S. Department of Energy, and supported in part by Michigan State University through computational resources provided by the Institute for Cyber-Enabled Research (iCER). The work of Z. F. and H. L. is partially supported by the US National Science Foundation under Grant No. PHY 1653405 ‘‘CAREER: Constraining Parton Distribution Functions for New-Physics Searches’’ and by the Research Corporation for Science Advancement through the Cottrell Scholar Award. The work of H. L. is partially supported by the US National Science Foundation under Grant No. PHY 2209424.

[1] Sayipjamal Dulat, Tie-Jiun Hou, Jun Gao, Marco Guzzi, Joey Huston, Pavel Nadolsky, Jon Pumplin, Carl Schmidt, Daniel Stump, and C.P. Yuan, New parton distribution functions from a global analysis of quantum chromodynamics, *Phys. Rev. D* **93**, 033006 (2016).

[2] L. A. Harland-Lang, A. D. Martin, P. Motylinski, and R. S. Thorne, Parton distributions in the LHC era: MMHT 2014 PDFs, *Eur. Phys. J. C* **75**, 204 (2015).

[3] R. D. Ball *et al.*, Parton distributions from high-precision collider data, *Eur. Phys. J. C* **77**, 663 (2017).

- [4] S. Alekhin, J. Blümlein, S. Moch, and R. Placakyte, Parton distribution functions, α_s , and heavy-quark masses for LHC Run II, *Phys. Rev. D* **96**, 014011 (2017).
- [5] A. Accardi, L. T. Brady, W. Melnitchouk, J. F. Owens, and N. Sato, Constraints on large- x parton distributions from new weak boson production and deep-inelastic scattering data, *Phys. Rev. D* **93**, 114017 (2016).
- [6] L. A. Harland-Lang, A. D. Martin, R. Nathvani, and R. S. Thorne, Ad Lucem: QED parton distribution functions in the MMHT framework, *Eur. Phys. J. C* **79**, 811 (2019).
- [7] Valerio Bertone, Stefano Carrazza, Nathan P. Hartland, and Juan Rojo, Illuminating the photon content of the proton within a global PDF analysis, *SciPost Phys.* **5**, 008 (2018).
- [8] Aneesh V. Manohar, Paolo Nason, Gavin P. Salam, and Giulia Zanderighi, The photon content of the proton, *J. High Energy Phys.* **12** (2017) 046.
- [9] Serguei Chatrchyan *et al.*, A new boson with a mass of 125 GeV observed with the CMS experiment at the large hadron collider, *Science* **338**, 1569 (2012).
- [10] Roman Kogler *et al.*, Jet substructure at the large hadron collider: Experimental review, *Rev. Mod. Phys.* **91**, 045003 (2019).
- [11] A. Accardi *et al.*, Electron ion collider: The next QCD frontier: Understanding the glue that binds us all, *Eur. Phys. J. A* **52**, 268 (2016).
- [12] J. Arrington *et al.*, Revealing the structure of light pseudoscalar mesons at the electron-ion collider, *J. Phys. G* **48**, 075106 (2021).
- [13] Arlene C. Aguilar *et al.*, Pion and Kaon structure at the electron-ion collider, *Eur. Phys. J. A* **55**, 190 (2019).
- [14] R. Abdul Khalek *et al.*, Science requirements and detector concepts for the electron-ion collider: EIC yellow report, *Nucl. Phys. A* **1026**, 122447 (2021).
- [15] Huey-Wen Lin *et al.*, Parton distributions and lattice QCD calculations: A community white paper, *Prog. Part. Nucl. Phys.* **100**, 107 (2018).
- [16] Martha Constantinou *et al.*, Parton distributions and lattice-QCD calculations: Toward 3D structure, *Prog. Part. Nucl. Phys.* **121**, 103908 (2021).
- [17] M. Gockeler, R. Horsley, Ernst-Michael Ilgenfritz, H. Oelrich, H. Perlt, Paul E. L. Rakow, G. Schierholz, A. Schiller, and P. Stephenson, A preliminary lattice study of the glue in the nucleon, *Nucl. Phys. B, Proc. Suppl.* **53**, 324 (1997).
- [18] K. F. Liu *et al.*, Quark and glue momenta and angular momenta in the proton—A lattice calculation, *Proc. Sci. LATTICE2011* (2011) 164.
- [19] R. Horsley, R. Millo, Y. Nakamura, H. Perlt, D. Pleiter, P. E. L. Rakow, G. Schierholz, A. Schiller, F. Winter, and J. M. Zanotti, A lattice study of the glue in the nucleon, *Phys. Lett. B* **714**, 312 (2012).
- [20] M. Deka *et al.*, Lattice study of quark and glue momenta and angular momenta in the nucleon, *Phys. Rev. D* **91**, 014505 (2015).
- [21] Constantia Alexandrou, Martha Constantinou, Kyriakos Hadjiyiannakou, Karl Jansen, Haralambos Panagopoulos, and Christian Wiese, Gluon momentum fraction of the nucleon from lattice QCD, *Phys. Rev. D* **96**, 054503 (2017).
- [22] C. Alexandrou, M. Constantinou, K. Hadjiyiannakou, K. Jansen, C. Kallidonis, G. Koutsou, A. Vaquero Avilés-Casco, and C. Wiese, Nucleon Spin and Momentum Decomposition Using Lattice QCD Simulations, *Phys. Rev. Lett.* **119**, 142002 (2017).
- [23] P. E. Shanahan and W. Detmold, Gluon gravitational form factors of the nucleon and the pion from lattice QCD, *Phys. Rev. D* **99**, 014511 (2019).
- [24] Yi-Bo Yang, Ming Gong, Jian Liang, Huey-Wen Lin, Keh-Fei Liu, Dimitra Pefkou, and Phiala Shanahan, Nonperturbatively renormalized glue momentum fraction at the physical pion mass from lattice QCD, *Phys. Rev. D* **98**, 074506 (2018).
- [25] C. Alexandrou, S. Bacchio, M. Constantinou, J. Finkenrath, K. Hadjiyiannakou, K. Jansen, G. Koutsou, H. Panagopoulos, and G. Spanoudes, Complete flavor decomposition of the spin and momentum fraction of the proton using lattice QCD simulations at physical pion mass, *Phys. Rev. D* **101**, 094513 (2020).
- [26] Yi-Bo Yang, Jian Liang, Yu-Jiang Bi, Ying Chen, Terrence Draper, Keh-Fei Liu, and Zhaofeng Liu, Proton Mass Decomposition from the QCD Energy Momentum Tensor, *Phys. Rev. Lett.* **121**, 212001 (2018).
- [27] Gen Wang, Yi-Bo Yang, Jian Liang, Terrence Draper, and Keh-Fei Liu, Proton momentum and angular momentum decompositions with overlap fermions, *Phys. Rev. D* **106**, 014512 (2022).
- [28] Ian Balitsky, Wayne Morris, and Anatoly Radyushkin, Gluon pseudo-distributions at short distances: Forward case, *Phys. Lett. B* **808**, 135621 (2020).
- [29] Jian-Hui Zhang, Xiangdong Ji, Andreas Schäfer, Wei Wang, and Shuai Zhao, Accessing Gluon Parton Distributions in Large Momentum Effective Theory, *Phys. Rev. Lett.* **122**, 142001 (2019).
- [30] Wei Wang, Jian-Hui Zhang, Shuai Zhao, and Ruilin Zhu, A complete matching for quasi-distribution functions in large momentum effective theory, *Phys. Rev. D* **100**, 074509 (2019).
- [31] Zhou-You Fan, Yi-Bo Yang, Adam Anthony, Huey-Wen Lin, and Keh-Fei Liu, Gluon Quasi-Parton-Distribution Functions from Lattice QCD, *Phys. Rev. Lett.* **121**, 242001 (2018).
- [32] Zhouyou Fan, Rui Zhang, and Huey-Wen Lin, Nucleon gluon distribution function from $2+1+1$ -flavor lattice QCD, *Int. J. Mod. Phys. A* **36**, 2150080 (2021).
- [33] Zhouyou Fan and Huey-Wen Lin, Gluon parton distribution of the pion from lattice QCD, *Phys. Lett. B* **823**, 136778 (2021).
- [34] Tanjib Khan *et al.*, Unpolarized gluon distribution in the nucleon from lattice quantum chromodynamics, *Phys. Rev. D* **104**, 094516 (2021).
- [35] Alejandro Salas-Chavira, Zhouyou Fan, and Huey-Wen Lin, First glimpse into the Kaon Gluon parton distribution using lattice QCD, *Phys. Rev. D* **106**, 094510 (2022).
- [36] E. Follana, Q. Mason, C. Davies, K. Hornbostel, G. P. Lepage, J. Shigemitsu, H. Trotter, and K. Wong, Highly improved staggered quarks on the lattice, with applications to charm physics, *Phys. Rev. D* **75**, 054502 (2007).
- [37] A. Bazavov *et al.*, Lattice QCD ensembles with four flavors of highly improved staggered quarks, *Phys. Rev. D* **87**, 054505 (2013).

- [38] Rajan Gupta, Yong-Chull Jang, Huey-Wen Lin, Boram Yoon, and Tanmoy Bhattacharya, Axial vector form factors of the nucleon from lattice QCD, *Phys. Rev. D* **96**, 114503 (2017).
- [39] Tanmoy Bhattacharya, Vincenzo Cirigliano, Saul Cohen, Rajan Gupta, Anosh Joseph, Huey-Wen Lin, and Boram Yoon, Iso-vector and iso-scalar tensor charges of the nucleon from lattice QCD, *Phys. Rev. D* **92**, 094511 (2015).
- [40] Tanmoy Bhattacharya, Vincenzo Cirigliano, Rajan Gupta, Huey-Wen Lin, and Boram Yoon, Neutron Electric Dipole Moment and Tensor Charges from Lattice QCD, *Phys. Rev. Lett.* **115**, 212002 (2015).
- [41] Tanmoy Bhattacharya, Saul D. Cohen, Rajan Gupta, Anosh Joseph, Huey-Wen Lin, and Boram Yoon, Nucleon charges and electromagnetic form factors from $2 + 1 + 1$ -flavor lattice QCD, *Phys. Rev. D* **89**, 094502 (2014).
- [42] Santanu Mondal, Rajan Gupta, Sungwoo Park, Boram Yoon, Tanmoy Bhattacharya, and Huey-Wen Lin, Moments of nucleon isovector structure functions in $2 + 1 + 1$ -flavor QCD, *Phys. Rev. D* **102**, 054512 (2020).
- [43] Anna Hasenfratz and Francesco Knechtli, Flavor symmetry and the static potential with hypercubic blocking, *Phys. Rev. D* **64**, 034504 (2001).
- [44] Gunnar S. Bali, Bernhard Lang, Bernhard U. Musch, and Andreas Schäfer, Novel quark smearing for hadrons with high momenta in lattice QCD, *Phys. Rev. D* **93**, 094515 (2016).
- [45] G. Martinelli, C. Pittori, Christopher T. Sachrajda, M. Testa, and A. Vladikas, A general method for nonperturbative renormalization of lattice operators, *Nucl. Phys.* **B445**, 81 (1995).
- [46] Yi-Bo Yang, Michael Glatzmaier, Keh-Fei Liu, and Yong Zhao, The 1-loop correction of the QCD energy momentum tensor with the overlap fermion and HYP smeared Iwasaki gluon, [arXiv.1612.02855](https://arxiv.org/abs/1612.02855).
- [47] Florian Herren and Matthias Steinhauser, Version 3 of RunDec and CRunDec, *Comput. Phys. Commun.* **224**, 333 (2018).
- [48] Barbara Schmidt and Matthias Steinhauser, CRunDec: A C++ package for running and decoupling of the strong coupling and quark masses, *Comput. Phys. Commun.* **183**, 1845 (2012).
- [49] K. G. Chetyrkin, Johann H. Kuhn, and M. Steinhauser, RunDec: A mathematica package for running and decoupling of the strong coupling and quark masses, *Comput. Phys. Commun.* **133**, 43 (2000).
- [50] Keh-Fei Liu, Jian Liang, and Yi-Bo Yang, Variance reduction and cluster decomposition, *Phys. Rev. D* **97**, 034507 (2018).
- [51] T. Blum *et al.*, Domain wall QCD with physical quark masses, *Phys. Rev. D* **93**, 074505 (2016).
- [52] N. Sato, C. Andres, J.J. Ethier, and W. Melnitchouk, Strange quark suppression from a simultaneous Monte Carlo analysis of parton distributions and fragmentation functions, *Phys. Rev. D* **101**, 074020 (2020).
- [53] Tie-Jiun Hou *et al.*, New CTEQ global analysis of quantum chromodynamics with high-precision data from the LHC, *Phys. Rev. D* **103**, 014013 (2021).
- [54] H. Abramowicz *et al.*, Combination of measurements of inclusive deep inelastic $e^\pm p$ scattering cross sections and QCD analysis of HERA data, *Eur. Phys. J. C* **75**, 580 (2015).
- [55] Robert G. Edwards and Balint Joo, The chroma software system for lattice QCD, *Nucl. Phys. B, Proc. Suppl.* **140**, 832 (2005).